

3D Printed Polyimide Nanocomposite Aerogels for Electromagnetic Interference Shielding and Thermal Management

Tingting Wu, Michal Ganobjak, Gilberto Siqueira,* Zhihui Zeng,* Mengmeng Li, Ekaterina Filimonova, Somayeh Saghmanesh, Anne Bonnin, Deeptanshu Sivaraman, Joshua Yip, Lei Li, Hui Wu, Gustav Nyström, Wim J. Malfait,* and Shanyu Zhao*


Aerogels were listed among the top ten emerging technologies in chemistry by IUPAC in 2022. Their record-breaking properties sparked the emergence of a thriving insulation market, but solutions are sought to promote additional applications. A 3D assembly process based on direct ink writing of “aerogel-in-aerogel” nanocomposites is presented. The printed polyimide-silica aerogels are non-brittle ($E = 6.7$ MPa) with a super-insulating thermal conductivity ($20.3 \text{ mW m}^{-1} \text{ K}^{-1}$) and high thermal stability ($T_{5\text{wt}\%} 447^\circ\text{C}$). In addition, they display excellent low-loss dielectric properties and microwave transmission over all relevant communication bands and can be functionalized for electromagnetic interference (EMI) shielding. The high shape-fidelity printing, combined with laser-induced etching of thermally conductive graphene layers, enable precise thermal management for portable electronics or maintain an extreme temperature gradient (-40 to $+50^\circ\text{C}$) across a millimeter-scale partition.

1. Introduction

Aerogels are highly porous solids obtained by replacing the liquid of gels with air without collapsing the microstructure,^[1] and display extraordinary properties including ultra-low thermal conductivity for thermal management^[2–4] and low dielectric permittivity for electrical insulation.^[5] They are difficult to machine because of the brittle nature, therefore present limited on-demand conformal capability and high cost for precise spatial design of pores and shapes. Additive manufacturing has endowed aerogels with designable and complex geometries toward customized applications.^[6–9] The

T. Wu, M. Ganobjak, M. Li, E. Filimonova, D. Sivaraman, J. Yip, W. J. Malfait, S. Zhao
Laboratory for Building Energy Materials and Components
Swiss Federal Laboratories for Materials Science and Technology
Empa
Dübendorf 8600, Switzerland
E-mail: wim.malfait@empa.ch; shanyu.zhao@empa.ch
G. Siqueira, G. Nyström
Cellulose & Wood Materials Laboratory
Swiss Federal Laboratories for Materials Science and Technology
Empa
Dübendorf 8600, Switzerland
E-mail: gilberto.siqueira@empa.ch
Z. Zeng
School of Materials Science and Engineering
Shandong University
Jinan 25006, P. R. China
E-mail: zhihui.zeng@sdu.edu.cn

M. Li
State Key Laboratory for Modification of Chemical Fibers and Polymer Materials
College of Materials Science and Engineering
Donghua University
Shanghai 201620, P. R. China
S. Saghmanesh
Center for X-ray Analytics
Swiss Federal Laboratories for Materials Science and Technology
Empa
Dübendorf 8600, Switzerland
A. Bonnin
Swiss Light Source
Paul Scherrer Institute
Villigen 5232, Switzerland
L. Li, H. Wu
State Key Laboratory of New Ceramics and Fine Processing
School of Materials Science and Engineering
Tsinghua University
Beijing 100084, P. R. China
G. Nyström
Department of Health Science and Technology
ETH Zürich
Zürich 8092, Switzerland

 The ORCID identification number(s) for the author(s) of this article can be found under <https://doi.org/10.1002/admt.202202155>

© 2023 The Authors. Advanced Materials Technologies published by Wiley-VCH GmbH. This is an open access article under the terms of the Creative Commons Attribution-NonCommercial-NoDerivs License, which permits use and distribution in any medium, provided the original work is properly cited, the use is non-commercial and no modifications or adaptations are made.

DOI: 10.1002/admt.202202155

combination of low thermal conductivity and versatile structural and component design increases the potential of the 3D printed aerogels for customized thermal management^[10,11] and catalysis.^[6] Reported processes for aerogel additive manufacturing include three or four steps: development of a printable ink formulation, which is the primary and key challenge, followed by 3D printing of the desired geometry, optional post-curing steps for solidification or chemical modification, and finally applying an appropriate drying technique to maintain the shape fidelity and pore structure.^[12]

Current 3D printed aerogels are limited because the material properties lack in important aspects, for example, the poor mechanical properties of silica aerogel^[6] or the low thermal stability and hygroscopicity in case of cellulose aerogels.^[13] Polyimide aerogels display an excellent combination of good mechanical properties, high thermal stability (up to 400 °C), low thermal conductivity and excellent dielectric properties, implying their potential as thermal insulators and/or dielectric substrates for batteries, antenna and radomes.^[14,15] A few studies report on the feasibility of additive manufacturing of polyimide aerogels, either by direct ink writing (DIW)^[16,17] or by photo-curing.^[18] However, these formulations are constrained by the low printing resolution, poor shape fidelity and high deformation, arising either from the thermal imidization process in aqueous poly(amic acid) systems, or from the low printability and short printing window in organic solvent based systems. Hence, a suitable rheology modifier to guarantee a stable printing process is critical for reliable polyimide aerogel printing. Silica aerogel particles have been verified as an efficient rheology modifier for DIW of silica aerogels.^[6] Moreover, the addition of silica aerogels into mold-cast polyimide aerogels has improved thermal conductivity ($17.5 \text{ mW m}^{-1} \text{ K}^{-1}$), thermal stability, and hydrophobicity.^[19]

Here, we present a method to 3D print poly(amic acid) (PAA)-silica inks with silica aerogel particles in a dual role as viscosity modifier and property enhancer. The ink shows a broad printing window and long-time rheological stability for DIW. A low thermal conductivity ($20.3 \text{ mW m}^{-1} \text{ K}^{-1}$) is achieved for the 3D printed polyimide-silica aerogels with high-temperature stability in terms of chemical composition, pore structure and geometrical shape, attributed to the addition of silica aerogel fillers. The thermal managements in extreme conditions and electronics are demonstrated based on the obtained low thermal conductivity and the superb printability.

2. Results and Discussion

2.1. Additive Manufacturing of Polyimide Aerogel Composites

PAA was first polymerized from 3,3',4,4'-biphenyl tetracarboxylic dianhydride (BPDA), 4,4'-oxydianiline (ODA) and 2,2'-dimethylbenzidine (DMBZ), and afterward cross-linked by 1,3,5-benzenetricarbonyl trichloride (BTC).^[20] PAA is soluble in dimethylacetamide (DMAc), whose low vapor pressure prevents premature drying during printing, and can be chemically imidized into polyimide once the completion of 3D printing to cure and maintain the complex geometry (Figure 1a). The vapor pressure of DMAc is 300 Pa at 20 °C, which is about 12 times lower than water. For the DIW, the low vapor pressure of the solvent used in the ink preparation is critical to prevent the drying

of the printed objects before the post treatments and supercritical CO₂ drying. In Figure 1a, the purple part is the specific chemical structure of poly(amic acid) used in this work, and the green part is the corresponding polyimide. The Figure 1b shows the general preparation process of this work, where the purple and green parts show the general chemical structure of poly(amic acid) and polyimide, R_1 represents the rest of the chemical structure of dianhydride and R_2 represents the rest of the chemical structure of diamine. Silica aerogel particles (4–20 μm, Figure S1, Supporting Information) were incorporated into the PAA solution to: i) modify the ink rheology to enable DIW; and ii) improve the composite aerogel properties.^[19] All ink formulations show a similar shear thinning behavior (Figure 1e), but strongly variable storage moduli and yield stresses depending on the filler concentration (Figure S2, Supporting Information). The optimal silica concentration (9.0 wt% or ≈60 vol%) imparts the ink with a yield stress of 1440 Pa (Figure 1d), appropriate to retain complex and self-supporting geometries (overhang up to 45°, Figure 1c, and Movie S1, Supporting Information), which is essential because of the post-curing approach adopted. Compared to often reported sol-gel printing strategies with continuously changing rheological properties, that is, where printing takes place at the onset or during gelation, the post-printing curing trigger developed here, based on simultaneously vapor-induced curing and chemical imidization with acetic anhydride and pyridine vapor, extends the printing times, enables printing of larger objects and provides consistent printing quality. The obtained polyimide chemical structure was confirmed to correspond to the one shown in Figure 1a through FTIR (Figure S3, Supporting Information), and by solid-state NMR spectroscopy in our previous work.^[19] The imidized gels were first solvent exchanged from toxic DMAc to ethanol, which owns higher miscibility with the final drying solvent supercritical CO₂. After the supercritical CO₂ drying (Figure 1b), the printed objects display continuous and straight filaments during the printing (Figure 1f,g), and low distortion and shrinkage after imidization, solvent exchange and drying (Figure 1h,j). The surface (Figure 1i) and cross-section (Figure 1j) of printed grids verify a good shape retention and homogeneous dispersion of silica aerogel particles in polyimide aerogel matrix. Further micro-CT images will be presented in the following part to prove the homogeneous dispersion of silica aerogel particles in the polyimide matrix.

2.2. Pore Structure, Strength Optimization, and Wettability of the Printed Polyimide Composites

The silica aerogel particles and the polyimide aerogel matrix are both mesoporous, with BET specific surface areas of 709 and 434 m² g⁻¹, respectively. The printed polyimide-silica aerogel composites display a BET specific surface area of 517 m² g⁻¹ and typical meso-porosity (Figure 2a, and Figure S4, Supporting Information), which confirms an apparent improvement due to the contribution of silica aerogels. The composites inherit the high temperature resistance from both silica and polyimide phases, with $T_{5wt\%}$ at 447 °C (Figure 2b). A filament printed through a 410 μm-nozzle displays moderate shrinkage of 12% with a final diameter of 350 μm (Figure 2d). The aerogel-in-aerogel structure of nanoparticulate silica aerogel grains embedded

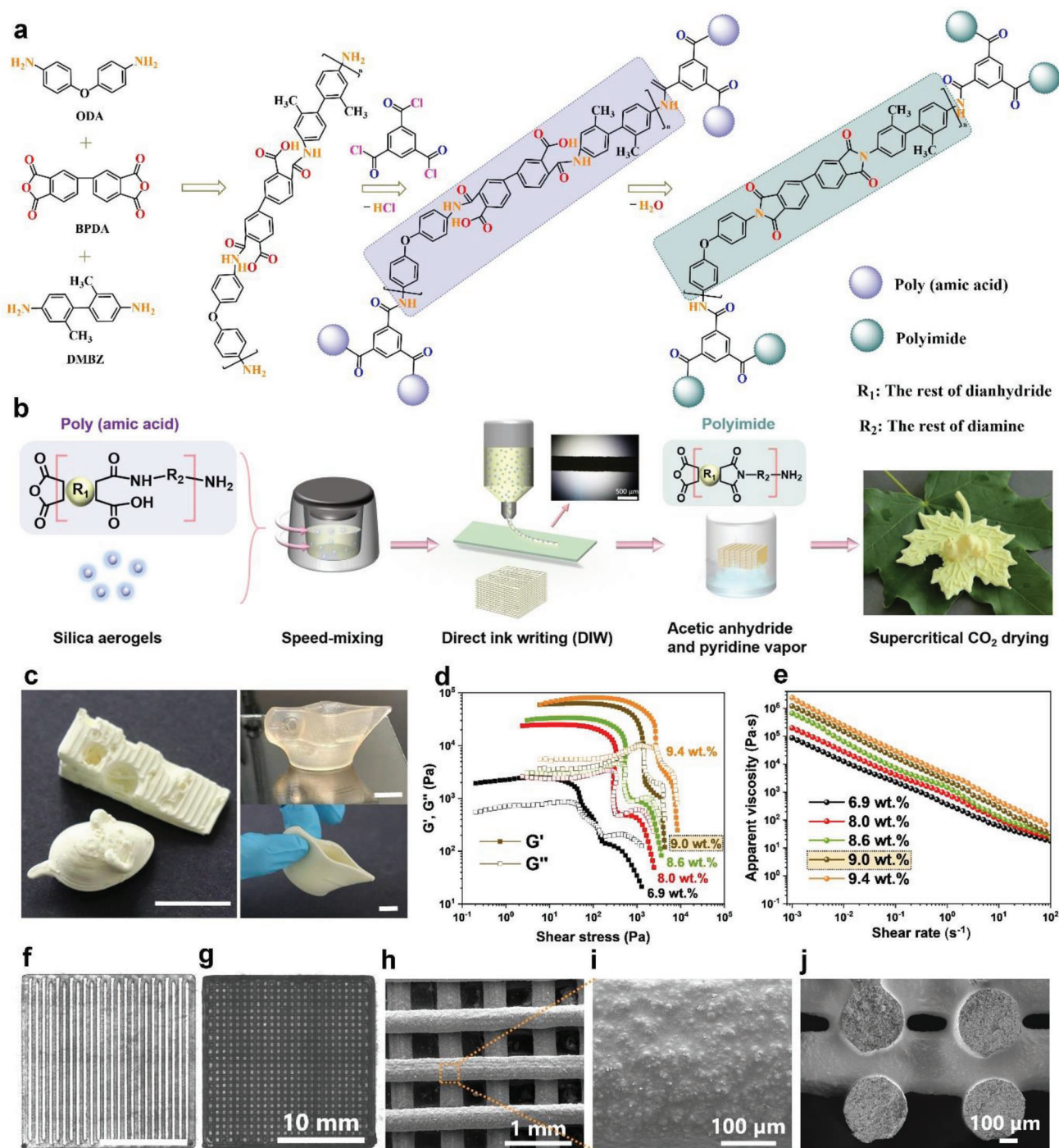


Figure 1. Ink preparation, rheology, and printing consistency. a) Polyimide synthesis from the monomers (BPDA, ODA, DMBZ) and cross-linker (BTC). b) DIW of polyimide-silica composite aerogels from a PAA-silica aerogel ink. c) Printed and dried objects (scale bar is 10 mm). d) Storage modulus (G') and loss modulus (G'') versus shear stress, and e) steady-shear rheological measurements of inks with different silica aerogel filler contents (6.9 wt%, 8.0 wt%, 8.6 wt%, 9.0 wt%, and 9.4 wt%). Photos taken during printing of f) a one-layer and g) a five-layer grid. SEM images of the h) dried grid and filaments, i) the surface of dried filament, and j) the cross-section of the dried grids.

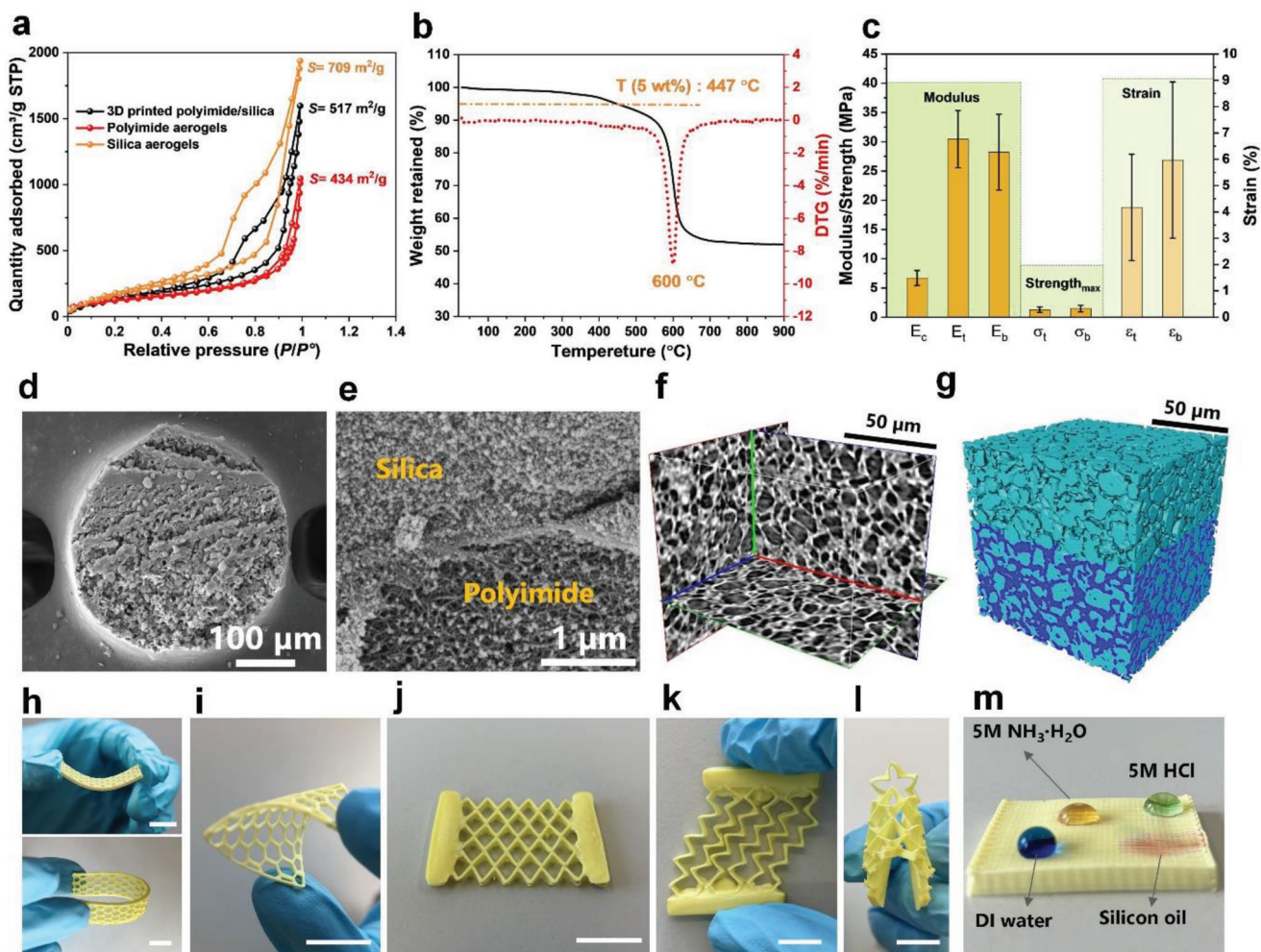


Figure 2. Properties of 3D printed, polyimide-silica aerogels. a) N_2 sorption isotherms of polyimide aerogel, silica aerogel powder and the 3D printed composite. b) Thermogravimetric analysis. c) Mechanical performance from compression, tensile, and 3-point bending tests. d) and e) SEM images of a dried filament cross-section. f) Orthogonal 2D cross-sections and g) 3D volume rendering with silica aerogel grains (light green, 60 vol%) embedded in polyimide aerogel matrix (dark blue, 40 vol%) ($100 \times 100 \times 100 \mu m^3$, effective voxel size of 162.5 nm). h–l) Flexibility of printed aerogels with optimized topologies (scale bar is 10 mm). m) Hydrophobicity and chemical resistance.

in a nanofibrillar polyimide aerogel matrix (Figure 2e) results from the homogeneous dispersion of silica aerogel grains in the polyimide aerogel matrix (Figure 2d–j, and Figures S5 and S6, Supporting Information). This homogeneity imparts the ink with a consistent rheology, enables high-shape fidelity printing, and gives the final aerogel its desirable properties. The interface between fibrous polyimide matrix and particulate silica aerogels shows the two-phase aerogel-in-aerogel structure (Figure 2e). This microstructure with a high meso-porosity in both phases, but particularly for the silica aerogel additive, results in a low thermal conductivity of $20.3 \text{ mW m}^{-1} \text{ K}^{-1}$ (Figure S7 and Movie S2, Supporting Information), lower than that of conventional polyimide aerogels ($25.0\text{--}50.0 \text{ mW m}^{-1} \text{ K}^{-1}$), representing the lowest record (Figure S8, Supporting Information).^[21]

The polyimide aerogel matrix compensates for the brittleness of silica aerogels^[2] and the composite aerogels display compressive, tensile and 3-point bending Young's moduli of 6.7 ± 1.3 , 30.4 ± 4.9 and $28.2 \pm 6.5 \text{ MPa}$, respectively (Figure 2c, and

Figure S9 and Movie S3, Supporting Information). The printed aerogels are robust and easy to handle, and can be compressed by up to 80% strain without any cracks, but have only limited ductility and bendability, with an elongation of 4.2% in tensile tests and 6.0% deformation in 3-point bending tests. The flexibility of the aerogel composites can be improved by reducing the silica aerogel fillers but with the deterioration of thermal insulation and high temperature stability. Alternatively, selecting a more flexible 4, 4'-oxydianiline, in replacing the rigid DMBZ, will allow for the improvement of structure flexibility. Taking advantage of the design freedom of additive manufacturing in the printable geometries, for example, 3D honeycomb or rhombus patterns, promotes us to obtain aerogels with optimized mechanical topologies (Figure 2h–l, and Movie S4, Supporting Information). The addition of hydrophobic silica aerogel enhances the hydrophobicity with stable water contact angles of 109° , and a humidity uptake of only 3.5 wt% at 90% relative humidity (Figure 2m, and Figure S10, Supporting Information).

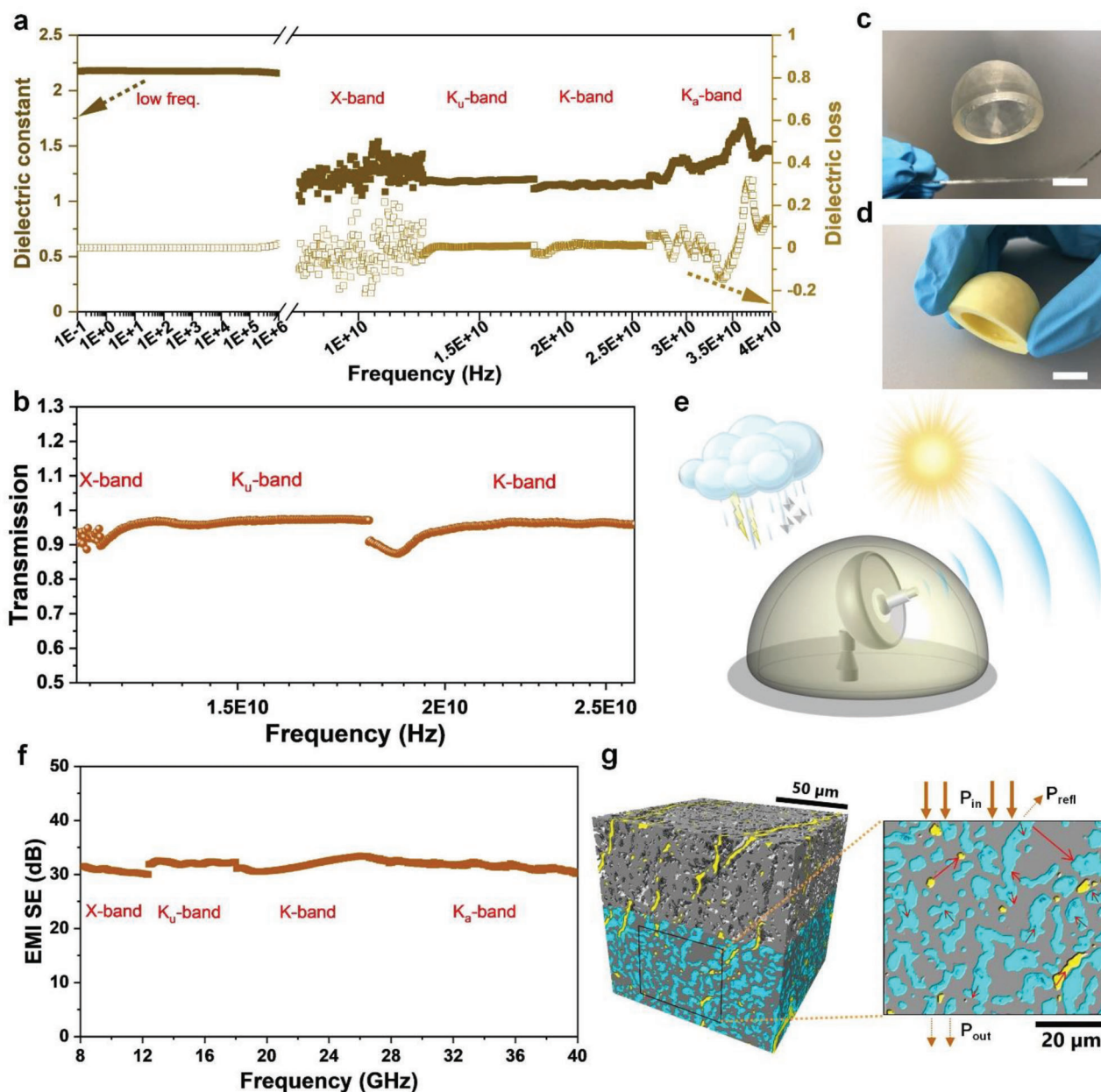


Figure 3. Dielectric properties, microwave transmission, and EMI SE of 3D printed polyimide/silica composite aerogels. a) Dielectric constant and dielectric loss at different frequencies. b) Micro-wave transmission. Printed (c) and dried (d) aerogel radome (scale bar is 10 mm). e) Illustration of polyimide-silica composite aerogel radomes. f) EMI SE of carbonized polyimide-silica-rGO composites (thickness: 2.92 mm). g) 3D rendering with silica aerogel grains (light green) embedded in carbonized polyimide matrix (gray) and rGO (yellow) ($100 \times 100 \times 100 \mu\text{m}^3$, effective voxel size of 162.5 nm); 2D image with arrows to demonstrate the possible shielding mechanism.

Moreover, the printed polyimide-silica aerogel composites are chemically resistant to aqueous acids and bases

2.3. Multifunctional Assembly for Dielectric and Electromagnetic Shielding

Polyimide aerogels generally have low dielectric constant because of the high porosity and intrinsic polyimide composition.^[5]

The addition of silica aerogel filler introduces the interfaces between silica aerogel and polyimide matrix but does not reduce the dielectric properties of printed composite aerogels (Figure 3a), due to its comparable or even higher porosity. In the low frequency range (10^{-1} to 10^6 Hz, radio wave and sub-microwave regions), the dielectric constant and loss are around 2.17 and 10^{-4} , respectively. In the X-band (8.2–12.4 GHz, microwave region), the dielectric constant and loss are around 1.00–1.50 and between ± 0.2 , respectively. In the even higher frequency of Ku-band

(12.4–18 GHz) and K-band (18–26 GHz), representative for radar or satellite communications, the dielectric constant and loss are around 1.15–1.17 and between -0.03 and 0.02 , respectively. In the super high Ka-band (26–40 GHz, for high Mach aircraft and aerospace communications), the dielectric constant and loss are around 1.20–1.72 and -0.15 to 0.30 , respectively. Consequently, over 90% microwave transmission (Figure 3b) was detected in the frequency range from 12 to 26 GHz. As a result, a good transparency at radio frequency indicates the non-disturbance of printed polyimide-silica aerogel radomes (Figure 3c,d, and Movie S5, Supporting Information), and the possibility for practical applications to protect the radar against harsh environments (Figure 3e).

After functionalization, the composite aerogels can also target the opposite application of wave transmission: reduced graphene oxide (rGO) and carbon nanotube (CNT) were added to the polyimide-silica aerogels together with the subsequent carbonization to impart a high electromagnetic interference (EMI) shielding effectiveness (SE) (Figure S11, Supporting Information). The carbonized composite aerogels functionalized with rGO display an EMI SE of 30–32 dB in the ultra-broadband gigahertz frequency range including X-band, Ku-band, K-band, and Ka-band (Figure 3f); an EMI specific SE (SSE) of 220–245 dB $\text{cm}^3 \text{g}^{-1}$ (Figure S12, Supporting Information). The high EMI SE results from the unique architecture consisting of a conductive rGO-doped carbonized polyimide scaffold around non-conductive silica aerogel grains, where the synergy of conductive loss and multiple reflections of incident electromagnetic waves effectively contribute to the attenuation of the waves (Figure 3g).^[22] The obtained carbonized composites include three phases: carbonized polyimide, silica aerogels and rGO, where the multiple interfaces between them play an important role in the electromagnetic wave attenuation behavior via the effect of interfacial attenuation.

2.4. Thermal Management in Extreme Conditions and Electronics

We have achieved efficient thermal management through pairing the low-thermal conductivity 3D printed polyimide-silica aerogels with a heat conductor. In the first thermal management example (Figure 4a–d, and Figure S13, Supporting Information), we 3D printed a thermally super-insulating aerogel object with complex geometrical channels, enabled by the high shape fidelity (Figure S14, Supporting Information). The negative space was subsequently filled with silver paste as a thermal conductor (Figure 4b). When placed on a hotplate at 220°C , the heat is conducted by the channels and the Empa logo is clearly visible in the infrared image (Figure S15, Supporting Information), implying the good thermal insulation and high thermal stability of the printed polyimide/silica composite aerogels at high service temperature. Alternatively, half of the logo was placed on a resistive heater, while the other half was connected to a liquid nitrogen sink (Figure S16, Supporting Information). A specific high-low temperatures pair ($+100$ and -50°C of the input temperatures) was selected to meet the detection limit of the Infrared camera. Thanks to the ultra-low thermal conductivity of the polyimide/silica composite aerogel, the temperature difference from $+50$ to -40°C could be maintained over an in-

sulation gap of 1 mm (Figure 4c,d), illustrating the power of precisely manufactured super-insulating materials for thermal management.

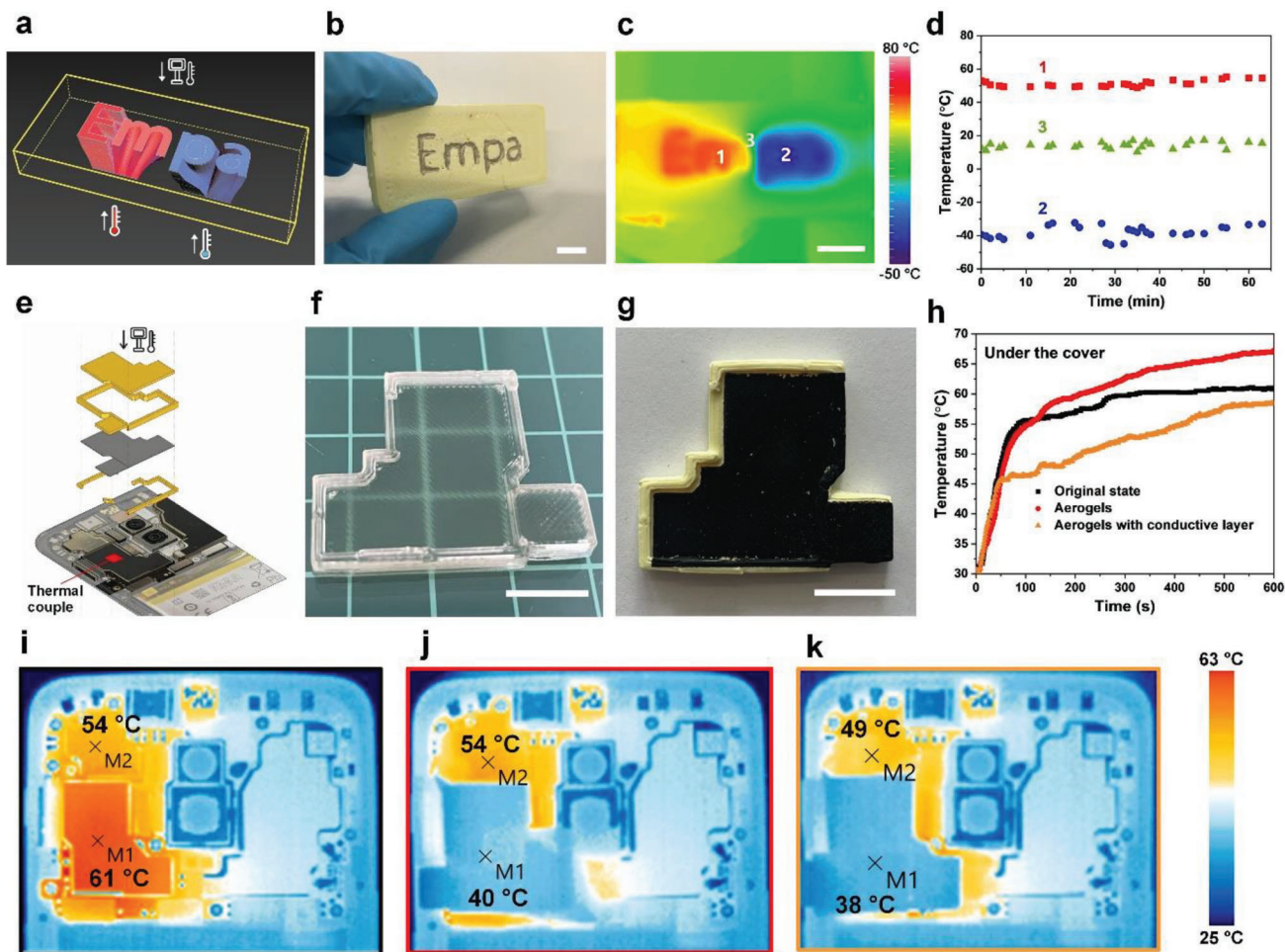
In the recent design of high power, highly integrated micro-electronics, 5G/6G smartphones in particular, the thermal dissipation always contains both heat conductor and thermal insulator to force the heat spread into two-dimension. This has already become a basic configuration,^[23] but it can only improve users' comfort and cannot effectively prevent the accumulation of heat in the smartphone. Therefore, the second thermal management example (Figure 4e–k, and Figure S17, Supporting Information) combines the custom design of a thermal superinsulator with a thermal conductor in a single composite to control and guide the heat dissipation direction. The goal in this smartphone application (Figure 4e, and Movie S6, Supporting Information) was to render the top of the insulator safe to touch and protect the surrounding heat-sensitive components, without overheating the component that is to be shielded. Although multi-material printing that combines an insulating and conductive ink is possible, we opted to etch a laser-induced, thermally conductive graphene layer on the surface of a printed polyimide-silica aerogel object (Figure 4f,g).^[24,25] After a 10 min operation, the temperature of the bare component increased to 61°C (Figure 4h). The use of a polyimide-silica aerogel shield decreased the temperature on top to 40°C , but the component itself ramped up to 67°C because the heat was trapped under the cover (Figure 4h). In contrast, the polyimide-silica aerogel cover with a laser-etched graphene layer simultaneously decreased the temperature on top to 38°C and that of the component to 58°C because of the spatially controlled application of a thermal superinsulator with a conductor. Therefore, the conductive graphene layer we have created on the inner surface of the 3D printed insulator have successfully guided the heat away, and simultaneously reduced the inner and surface temperature of the smartphone, not confining the heat inside the insulation case.

3. Conclusion

In summary, the PAA-silica inks display superior, stable, and consistent printability for DIW of polyimide-silica aerogels. The low vapor pressure of the solvent (DMAc) combined with a post-printing gas-phase induced curing and chemical imidization procedure allows for a broad printing window and enables the printing of large and complex geometries. Importantly, the unique aerogel-in-aerogel microstructure endows the printed aerogels with a combination of exceptional thermal, mechanical and dielectric properties that make practical applications under demanding conditions feasible, particularly when combined with multi-ink printing, functional particles, pyrolysis or laser-induced etching for further functionalization.

4. Experimental Section

Preparation of Poly(amic acid)-Silica Inks: The BPDA-ODA/DMBZ with 9 wt% silica aerogel particles was selected as the example for the synthetic process. In detail, first 0.5686 g ODA (Sigma) was added into DMAc (Chemie-Brunschwig), after dissolved completely, 1.6171 g BPDA (Sigma) was added, stirring for around 5 min. Then, 0.6029 g DMBZ (TCI) was



added inside the suspension for another 30 min to get homogeneous poly (amic acid) (PAA) oligomer solution, at the end 0.0324 g BTC (Sigma) was added into the system. In total, the volume of DMAC was 40 mL, where the concentration of PAA was 7 wt%. Afterward, 4 g silica aerogels (amorphous, 5–20 μm ; ENOVA, Cabot Aerogel) were added into the PAA solution, which was 9 wt% of the total system. The homogenization of the PAA and silica mixture was achieved by speed-mixing (speed-mixer, DAC 150.1 FVZ, FlackTek) successively at 1000 rpm for 1 min, 1500 rpm for 1 min and 2350 rpm for 2 min, which was repeated twice. Optionally, rGO and carbon nanotube (CNT) (diameters of 10–20 nm and length of 1–10 μm , Bayer Material Science) were added together with silica aerogels into the inks for multi-functionality.

Preparation of Reduced Graphene Oxide: Graphene oxide (GO) was prepared through a modified Hummer’s method and then freeze-dried.^[26] Obtained dry GO was reduced into rGO at 950 $^{\circ}\text{C}$ for 1 h under nitrogen atmosphere, where the ramping rate was 5 $^{\circ}\text{C min}^{-1}$.

Printing of Poly(amic acid)-Silica Inks: The homogenized ink was loaded into a cartridge for centrifuge at 3500 rpm for 15 min to remove the air bubble (Rotina 380, Hettich). Then the ink was ready and stored in 5 $^{\circ}\text{C}$ fridge for DIW. The cartridge was loaded in the printer (Bioplotter, Envision TEC) with conical nozzle (the diameters of nozzle selected in

this work were 410, 840, and 1190 μm ; smoothflow tapered tip, H. Sigrist & Partner). The inks were driven pneumatically through the nozzles with pressures ranging between 2.0 and 4.0 bar on a glass substrate (10 cm \times 10 cm), with a filament extrusion rate of 15–24 mm s^{-1} . Printing paths and STL files were generated by Magics Envisiontec 18.2, sliced, and converted into BPL files (Bioplotter RP software package) to command the x–y–z motion of the printer head.

Post-Curing and Drying: The printed objects were placed in a closed container with acetic anhydride (Lonza) and pyridine (Acros Organics) mixture, but not direct contact with the chemical imidizer for 2–4 h to fix the contour of the printed objects. Afterward the partially cured gels were directly put inside the chemical imidizer to make sure of full imidization. Then, the imidized polyimide-silica gels were stepwise solvent exchanged into ethanol (5% isopropanol, Alcosuisse) for supercritical CO_2 drying (SCF extractor, Separex).

Carbonization: The printed polyimide-silica composite aerogels were pyrolyzed at 900 $^{\circ}\text{C}$ for 2 h under nitrogen atmosphere, where the ramping rate was 5 $^{\circ}\text{C min}^{-1}$.

Particle Size Distribution: Silica aerogel particles were directly dispersed in DMAC, and then measured on a Beckmann Coulter particle size analyzer (LS 13 320).

Rheology: Rheometer (MCR 302 rheometer, Anton Paar) was used with a plate-plate (diameter of 25 mm) geometry with a gap of 0.5 mm. All the measurements were conducted at 20 °C. The inks with different silica aerogels loading amounts (3.0, 3.5, 3.8, 4.0 and 4.2 g, which were 6.9 wt%, 8.0 wt%, 8.6 wt%, 9.0 wt% and 9.4 wt%, respectively) were prepared for the rheological test in both rotation mode and amplitude sweeping mode. Storage and loss moduli were recorded with oscillatory strain variations from 0.01 to 1000% at a frequency of 1 Hz. The yield stress was defined as the shear stress where storage and loss moduli were equal. Viscosity was obtained by changing rotational shear rate from 0.001 to 1000 s⁻¹.

Identification of Chemical Structure: ATR-FTIR measurements were performed on a spectrometer from Bruker Switzerland AG with the ATR name Tensor 27 over the wavenumber range from 500 to 4000 cm⁻¹.

Microstructural Analysis: SEM images were acquired on a FEI Nova NanoSEM 230 at an accelerating voltage of 10 kV and a working distance of ≈5 mm. 15 nm of Pt (measured with a flat piezo detector) was coated to avoid charging prior to the measurement. Nitrogen sorption analysis was carried out on a nitrogen sorption analyzer (TriFlex, Micromeritics) after prior degassing for 15 h at 80 °C and 0.02 mbar. The specific surface areas (SBET, uncertainty ≈50 m² g⁻¹) were calculated by the Brunauer–Emmett–Teller (BET) method.

Thermal Stability: Thermogravimetric analysis was conducted on a Netzsch TG 209F1 Thermogravimetric Analyzer operating at 10 K min⁻¹ in air atmosphere.

Synchrotron X-Ray Tomographic Microscopy: Aerogel monoliths were cut and tested by micro/nano computed tomography. Imaging was performed at the TOMCAT beamline of the Swiss Light Source, situated on a 2.9 T bending magnet, and equipped with a multi-layer monochromator. X-ray images were acquired at 16 keV and a propagation distance of 25 mm. The X-ray indirect detector comprised a LSO:Tb 5.8 µm scintillator, a ×40 optical objective and a sCMOS pco.EDGE camera (6.5 µm pixel size, 2560 × 2160 pixels), resulting in an effective pixel size of 0.1625 µm. During the continuous tomography scan, 1500 projections were collected over 180° with an exposure time of 500 ms per projection as well as two series of 50 flats and a series of 20 dark projections. The data were reconstructed using the gridrec algorithm with and without prior phase-retrieval (Paganin, delta = 6.3e-6, beta = 3.6e-8 with unsharp mask of 0.3 width and sigma = 1). The reconstructed data were processed further through a non-local means filter in the Avizo 3D (Thermo Fisher Scientific, Germany, version 2021.2) software. The 3D denoising procedure was done on a GPU adaptive manifold mode of that filter with a spatial standard deviation of 4 pixels. The intensity standard deviation was set on 0.2 with a search window of 10 pixels and a local neighborhood of 3 pixels. After denoising, a region of 100 µm × 100 µm × 100 µm, free of CT reconstruction artifacts, was selected from the 3D image volume. The region-of-interest (ROI) volume was segmented through a thresholding process on gray values to separate the polymer, silica aerogel particles, and porosity. The polymer matrix appears as the hyper-intense (bright) signal on CT images due to its higher mass density than the silica aerogel particles, in which the latter could then be distinguished well by the hypo-intense signal (dark) signal. The porosity was the darkest signal on the image, consistent with the blank space gray value in the background. Then, the separated phases together with the whole segmented object were 3D rendered and visualized. All segmentation and visualization processes were performed in the Avizo software.

Mechanical Properties: Five identical cylinders (diameter was 8 mm, height was 13 mm) were printed for compression testing with an 840 µm nozzle, which were operated on a universal testing machine (Zwick 1484, Zwick GmbH, Germany) at a compression rate of 2 mm min⁻¹ up to 80% compressive strain. For tensile and 3-point bending test, AllroundLine universal testing machine Z005 by Zwick Roell equipped with a 5 kN load cell was used. Five dog-bone tensile samples were printed with a 410 µm nozzle at a rate of 5 mm min⁻¹. Five stripes (70 × 11 × 3 mm³) were printed with a 410 µm nozzle for 3-point bending test at a rate of 5 mm min⁻¹ with a support span length of 50 mm.

Hydrophobicity: The surface wettability of printed aerogels was evaluated by water contact angle measurement using a Contact Angle System OCA (Dataphysics TBU 90E, Germany), combined with a high-speed camera and a precision stainless steel tip (Gauge 32, EFD). The volume of the

water droplet was 10 µL. Dynamic water vapor sorption (DVS) isotherms were acquired using a dynamic water vapor sorption (DVS) Endeavour 5X Parallel Gravimetric Sorption Analyzer (Surface Measurement Systems). Around 50 mg printed aerogels were put onto the high-precision microbalance, allowing continuous monitoring of the weight of adsorbed water vapor once exposed to a stepwise increasing humidity (0–90%) in 5% increments with a controlled flow of mixture of nitrogen and water vapor. Prior to the measurement, aerogels were treated at 80 °C for 2 h under nitrogen atmosphere to remove the potential absorbed water. The resulting weight was taken as the dry reference. Afterward, the chamber cooled to 25 °C to collect the weight change at different humidities.

Thermal Conductivity: Thermal conductivities were determined from square plate aerogels (around 50 × 50 × 5 mm³, printed with a 1190 µm nozzle) using a custom-built guarded hot plate device (guarded zone: 50 × 50 mm², measuring zone: 25 × 25 mm²) designed for small samples of low thermal conductivity materials with a 10 °C temperature difference.^[27]

Dielectric Properties, Wave Transmission, and EMI Shielding: The waveguide transmission technique was employed for testing the dielectric properties of printed polyimide-silica aerogels. Five different frequency ranges were studied. For low-frequency measurements (10⁻¹ to 10⁶ Hz), the sample measurement was performed on a parallel plate capacitor using a Novocontrol impedance Alpha Analyzer combined with a Quatro temperature controller. Two stainless steel discs with a diameter of 20 mm served as electrodes. In the gigahertz frequency, the tests were performed using the waveguide method of a vector network analyzer (VNA, Agilent PNA N5244A). The sizes of the tested samples were 22.86 mm × 10.16 mm (length × width) in the frequency range of 8.2–12.4 GHz (X-band), 15.74 mm × 7.87 mm (length × width) in the frequency range of 12.4–18 GHz (Ku-band), 10.67 mm × 5.33 mm (length × width) in the frequency range of 18–26.5 GHz (K-band), and 7.12 mm × 3.56 mm (length × width) in the frequency range of 26.5–40 GHz (Ka-band), respectively. The S parameters were recorded and used to calculate the transmission and SE.^[28] The radome was printed with a 410 µm nozzle.

Infrared Thermal Imaging and Thermal Management: The infrared images in high temperature range were recorded using Testo 880–1 (measuring range 0–350 °C). Thermal couple (RS PRO RS-172TK Temperature & Humidity Data Logger) was used to record the temperature of cellphone. All the temperature and thermal images were recorded when the cellphone (Oneplus 6T) was running video call in filter mode. The thermal insulation performance with heat and cold source was evaluated using an infrared camera (TH 3102 MR, NEC-San-ei; measuring range –60 to 220 °C) equipped with a Stirling-cooled HgCdTe detector, with a temperature sensitivity of 0.08 at 30 °C and an accuracy of ±0.5 °C. The emission was set to 1. Thermal images were analyzed on a PicWin-IRIS system (version 7.3). The object with “Empa” thermal channeling was printed with an 840 µm nozzle.

Laser Etching Treatment: The cellphone cover was printed with a 410 µm nozzle. Afterward, the dried cellphone was etched to get a porous graphene layer using a CO₂ laser cutter (Nova24 60 W, Thunder Laser Tech Co., Ltd., Shatian, China) with 10% power and 200 mm s⁻¹ speed.

Supporting Information

Supporting Information is available from the Wiley Online Library or from the author.

Acknowledgements

The authors thank Beatrice Fischer for the thermogravimetric analysis, Stefanie B. Hauser for the FTIR measurements, Dorina M. Opris for the dielectric test in the frequency range of 10⁻¹ to 10⁶ Hz, Samuel Brunner for the setup of IR camera, and Thomas Bergmann for the help with supercritical drying. Somayeh Saghmanesh received funding from Co-fund EMPA POSTDOCS-II and EU Horizon 2020 under Marie Skłodowska-Curie agreement grant 754364.

Open access funding provided by ETH-Bereich Forschungsanstalten.

Conflict of Interest

The authors declare no conflict of interest.

Data Availability Statement

The data that support the findings of this study are available from the corresponding author upon reasonable request.

Keywords

additive manufacturing, aerogels, dielectric properties, polyimide, thermal management

Received: December 20, 2022
Revised: March 7, 2023
Published online: April 2, 2023

- [1] S. S. Kistler, *Nature* **1931**, 127, 741.
- [2] T. Linhares, M. T. Pessoa De Amorim, L. Durães, *J. Mater. Chem. A* **2019**, 7, 22768.
- [3] L. Su, H. Wang, M. Niu, S. Dai, Z. Cai, B. Yang, H. Huan, X. Pan, *Sci. Adv.* **2020**, 6, 1.
- [4] Y. Si, X. Wang, L. Dou, J. Yu, B. Ding, *Sci. Adv.* **2018**, 4, 1.
- [5] T. Wu, J. Dong, F. Gan, Y. Fang, X. Zhao, Q. Zhang, *Appl. Surf. Sci.* **2018**, 440, 595.
- [6] S. Zhao, G. Siqueira, S. Drdova, D. Norris, C. Ubert, A. Bonnin, S. Galmarini, M. Ganobjak, Z. Pan, S. Brunner, G. Nyström, J. Wang, M. M. Koebel, W. J. Malfait, *Nature* **2020**, 584, 387.
- [7] J. Feng, B. L. Su, H. Xia, S. Zhao, C. Gao, L. Wang, O. Ogbeide, J. Feng, T. Hasan, *Chem. Soc. Rev.* **2021**, 50, 3842.
- [8] Q. Cheng, Z. Sheng, Y. Wang, J. Lyu, X. Zhang, *ACS Nano* **2022**, 16, 4905.
- [9] L. An, Z. Guo, Z. Li, Y. Fu, Y. Hu, Y. Huang, F. Yao, C. Zhou, S. Ren, *Nat. Commun.* **2022**, 13, 1.
- [10] P. Guo, L. Su, K. Peng, D. Lu, L. Xu, M. Li, H. Wang, *ACS Nano* **2022**, 16, 6625.

- [11] L. Wang, J. Feng, Y. Luo, Z. Zhou, Y. Jiang, X. Luo, L. Xu, L. Li, J. Feng, *ACS Appl. Mater. Interfaces* **2021**, 13, 40964.
- [12] H. Tetik, Y. Wang, X. Sun, D. Cao, N. Shah, H. Zhu, F. Qian, D. Lin, *Adv. Funct. Mater.* **2021**, 31, 1.
- [13] T. Li, J. Song, X. Zhao, Z. Yang, G. Pastel, S. Xu, C. Jia, J. Dai, C. Dai, A. Gong, F. Jiang, Y. Yao, T. Fan, B. Yang, L. Wågberg, R. Yang, L. Hu, *Sci. Adv.* **2018**, 4, 1.
- [14] N. Leventis, C. Sotiriou-Leventis, D. P. Mohite, Z. J. Larimore, J. T. Mang, G. Churu, H. Lu, *Chem. Mater.* **2011**, 23, 2250.
- [15] Y. Cheng, X. Li, Y. Qin, Y. Fang, G. Liu, Z. Wang, J. Matz, P. Dong, J. Shen, M. Ye, *Sci. Adv.* **2021**, 7, 1.
- [16] C. Feng, S. S. Yu, *Polymers* **2021**, 13, 3614.
- [17] J. Yang, H. Wang, B. Zhou, J. Shen, Z. Zhang, A. Du, *Langmuir* **2021**, 37, 2129.
- [18] J. Herzberger, V. Meenakshisundaram, C. B. Williams, T. E. Long, *ACS Macro Lett.* **2018**, 7, 493.
- [19] Z. Kantor, T. Wu, Z. Zeng, S. Gaan, S. Lehner, M. Jovic, A. Bonnin, Z. Pan, Z. Mazrouei-Sebdani, D. M. Opris, M. M. Koebel, W. J. Malfait, S. Zhao, *Chem. Eng. J.* **2022**, 443, 136401.
- [20] M. A. B. Meador, C. R. Alemán, K. Hanson, N. Ramirez, S. L. Vivod, N. Wilmoth, L. McCorkle, *ACS Appl. Mater. Interfaces* **2015**, 7, 1240.
- [21] X. Li, J. Wang, Y. Zhao, X. Zhang, *ACS Appl. Mater. Interfaces* **2018**, 10, 16901.
- [22] D. X. Yan, H. Pang, B. Li, R. Vajtai, L. Xu, P. G. Ren, J. H. Wang, Z. M. Li, *Adv. Funct. Mater.* **2015**, 25, 559.
- [23] W. A. C. Hooton, E. Lee, M. Rammah, J. A. Bertin, S. P. Hristov, *Thermally Conductive Structure for Dissipating Heat in a Portable Electronic Device*, **2020**, 10, 787,014.
- [24] A. F. Carvalho, A. J. S. Fernandes, C. Leitão, J. Deuermeier, A. C. Marques, R. Martins, E. Fortunato, F. M. Costa, *Adv. Funct. Mater.* **2018**, 28, 1805271.
- [25] M. R. Bobinger, F. J. Romero, A. Salinas-Castillo, M. Becherer, P. Lugli, D. P. Morales, N. Rodríguez, A. Rivadeneyra, *Carbon* **2019**, 144, 116.
- [26] Z. Zeng, C. Wang, Y. Zhang, P. Wang, S. I. Seyed Shahabadi, Y. Pei, M. Chen, X. Lu, *ACS Appl. Mater. Interfaces* **2018**, 10, 8205.
- [27] S. Zhao, W. J. Malfait, A. Demilecamps, Y. Zhang, S. Brunner, L. Huber, P. Tingaut, A. Rigacci, T. Budtova, M. M. Koebel, *Angew. Chem.* **2015**, 127, 14490.
- [28] Z. Zeng, H. Jin, M. Chen, W. Li, L. Zhou, Z. Zhang, *Adv. Funct. Mater.* **2016**, 26, 303.